Adaptive time-lapse optimized survey design for electrical resistivity tomography monitoring

Paul B. Wilkinson,[1] Sebastian Uhlemann,[1,2] Philip I. Meldrum,[1]
Jonathan E. Chambers,[1] Simon Carrière,[1,3] Lucy S. Oxby[1] and M.H. Loke[4]

[1]*British Geological Survey, Environmental Science Centre, Keyworth, Nottingham NG*12 5*GG, United Kingdom. E-mail:* *pbw@bgs.ac.uk*
[2]*ETH-Swiss Federal Institute of Technology, Institute of Geophysics, Zurich, Switzerland*
[3]*Université Grenoble Alpes, ISTerre, F-38041 Grenoble, France*
[4]*Geotomo Software,* 115 *Cangkat Minden Jalan* 5*, Minden Heights,* 11700 *Gelugor, Penang, Malaysia*

SUMMARY

Adaptive optimal experimental design methods use previous data and results to guide the choice and design of future experiments. This paper describes the formulation of an adaptive survey design technique to produce optimal resistivity imaging surveys for time-lapse geo-electrical monitoring experiments. These survey designs are time-dependent and, compared to dipole–dipole or static optimized surveys that do not change over time, focus a greater degree of the image resolution on regions of the subsurface that are actively changing. The adaptive optimization method is validated using a controlled laboratory monitoring experiment comprising a well-defined cylindrical target moving along a trajectory that changes its depth and lateral position. The algorithm is implemented on a standard PC in conjunction with a modified automated multichannel resistivity imaging system. Data acquisition using the adaptive survey designs requires no more time or power than with comparable standard surveys, and the algorithm processing takes place while the system batteries recharge. The results show that adaptively designed optimal surveys yield a quantitative increase in image quality over and above that produced by using standard dipole–dipole or static (time–independent) optimized surveys.

Key words: Inverse theory; Tomography; Electrical properties; Hydrogeophysics.

1 INTRODUCTION

The development and introduction of remote automated multi-electrode instrumentation has facilitated geoelectrical monitoring of process-related problems at previously unprecedented spatial and temporal resolutions. Applications of electrical resistivity tomography (ERT) monitoring include landslides (Wilkinson *et al.* 2010a; Supper *et al.* 2014), engineered earthworks (Sjödahl *et al.* 2009; Chambers *et al.* 2014), tracer tests (Wilkinson *et al.* 2010b; Coscia *et al.* 2011), permafrost (Hilbich *et al.* 2011) and CO_2 sequestration (Kiessling *et al.* 2010). The use of permanently deployed systems with large numbers of electrodes has also been invaluable for testing statistical experimental design (SED) methods to generate optimized surveys that outperform traditional measurement schemes (Wilkinson *et al.* 2012a). Such methods are becoming more common in geophysics (Maurer *et al.* 2010) and have been applied to ERT (Stummer *et al.* 2004; Wilkinson *et al.* 2012a; Loke *et al.* 2014b), electromagnetics (Maurer *et al.* 2000; Myer *et al.* 2012; Roux & Garcia 2014), seismic tomography (Ajo-Franklin 2009), amplitude versus offset seismics (Guest & Curtis 2009) and seismic profiling (Shang & Huang 2012). However, these techniques are al-

most entirely used to create survey designs that are static over time. Some algorithms incorporate prior knowledge of the subsurface (Nenna *et al.* 2011), which could be derived from the interpretation of already acquired data (Coles & Morgan 2009; Khodja *et al.* 2010), but once designed, subsequent changes in the region being monitored have not previously been used to modify the measurements made in future iterations.

It should be noted that in the context of SED, the term 'sequential' is used to refer to both iterative algorithms for the creation of static experimental designs (Coles & Prange 2012) and techniques where data from previous experiments inform the design of the next (Guest & Curtis 2009). Rather than 'sequential', for clarity we will refer to the former as 'iterative' and the latter as 'adaptive'. Adaptive experimental design methods have been applied in disciplines other than geophysics. They are relatively well established in process engineering for parameter estimation problems (Franceschini & Macchietto 2008; Alaeddini *et al.* 2013) and have been used to control dose allocations and sampling schedules in clinical trials (Zamuner *et al.* 2010) and medical imaging studies (Xie *et al.* 2010). More closely related to environmental monitoring, adaptive design methods have been applied to determine how best to redistribute

or augment sensor networks in response to moving contamination (Uciński & Patan 2010; de Bruin *et al.* 2012). Adaptive optimal survey design was first posited in a geoelectrical monitoring context by Stummer *et al.* (2002). Coles & Morgan (2009) demonstrated that small ERT measurement sets can be augmented optimally based on the inversion of the data already acquired, but Wilkinson *et al.* (2012b) showed that for larger, more typical, sized surveys, the performance of optimal survey designs did not depend strongly on the assumed subsurface resistivity structure. But even though changes in the resistivity distribution should not adversely affect the optimality of a survey design, the changes themselves are of interest if they result from processes that are being investigated with ERT monitoring. Using optimal survey design it is possible to enhance resolution within targeted regions of a geophysical image (Khodja *et al.* 2010), which leads to the possibility of employing adaptive design methods to obtain extra information within, and hence to better resolve, dynamic regions of change caused by subsurface processes.

In this paper we present, to our knowledge, the first demonstration of adaptive optimized geophysical monitoring. We modify an existing static iterative design algorithm so that it can adaptively focus extra resolution within target regions of the image. We then use image analysis techniques to determine which regions of the subsurface have changed significantly within the preceding tomographic image, and enhance the resolution within these regions for the acquisition of the next data set. This technique is implemented using an existing automated ERT monitoring system with modified control software. We test the system and the adaptive optimization algorithm using a controlled, repeatable laboratory tank experiment with a dynamic target, and compare the image quality against results obtained using standard dipole–dipole and static optimized surveys.

2 OPTIMIZED ERT SURVEY DESIGN

The adaptive survey design algorithm studied in this paper is based on, and assessed relative to, the 'Compare *R*' (CR) method for optimizing static survey designs that we have developed in previous work. This method generates ERT surveys that give higher model resolution than standard survey designs for the same experimental cost. It has been shown, in numerical simulations, laboratory experiments and field studies, that it reliably produces subsurface geoelectrical images that are more accurate than those obtained from comparable standard surveys (Wilkinson *et al.* 2006, 2012a; Loke *et al.* 2010a,b, 2014a,b, 2015). The particular variant considered in this paper is able to make efficient use of multichannel resistivity instruments. The method is outlined below, but full details can be found in Wilkinson *et al.* (2012a), and the most efficient implementation of the core numerical calculations is described in Loke *et al.* (2015).

The CR method depends on an estimate of the model resolution matrix **R** for the linearized iterative Gauss–Newton solution to the ERT inverse problem (LaBrecque *et al.* 1996). This is given by

$$\mathbf{R} = (\mathbf{G}^{\mathrm{T}}\mathbf{G} + \mathbf{C})^{-1}\mathbf{G}^{\mathrm{T}}\mathbf{G}, \tag{1}$$

where the Jacobian matrix **G** comprises the logarithmic sensitivities of the measurements to changes in the model cell resistivities and the constraint matrix **C** contains the damping factors and roughness filters (Menke 1989). In this paper, the constraint matrix was chosen to represent a simple damped (Levenberg–Marquardt) least-squares problem, $\mathbf{C} = \lambda\mathbf{I}$ (Loke *et al.* 2010b). The matrix elements R_j on the leading diagonal of **R**, which we call the 'model resolution', lie

in the range $0 \leq R_j \leq 1$ (Wilkinson *et al.* 2006). A model resolution of $R_j = 0$ implies that the *j*th model cell is completely unresolved by the data and $R_j = 1$ implies that the *j*th model cell is perfectly resolved. The model resolution is maximal throughout the image space for the 'comprehensive' measurement set, which comprises all possible unique four-electrode measurements subject to a maximum geometric factor and measurement stability considerations (Wilkinson *et al.* 2012a; Loke *et al.* 2014b). The quality of any other given survey design (set of measurements) is assessed by examining its 'relative model resolution', $R_{\mathrm{r}} = R/R_{\mathrm{c}}$, where R_{c} is the model resolution for the comprehensive set.

The algorithm begins with a small predefined base set of measurement configurations and iteratively augments this with a smaller number of additional measurements that produce the greatest increase in its average relative model resolution:

$$S = \frac{1}{m} \sum_{j=1}^{m} \frac{R_j}{R_{\mathrm{c}j}}, \tag{2}$$

where *m* is the number of model cells. These additional configurations are selected subject to their sensitivity distributions having at least a given degree of mutual linear independence, and their effective use of a specified number of multichannel commands when combined with the base set. For the purposes of this paper, we define a multichannel command as a combination of *M* four-electrode configurations in which all configurations share the same current electrodes, adjacent configurations share a common potential electrode, and no potential electrode is used more than once. An *M*-channel command will therefore involve two current electrodes and $M + 1$ potential electrodes.

Once the multichannel survey has been designed, it has to be reordered to avoid electrode polarization errors (Dahlin 2000; Merriam 2005). These occur whenever a metallic electrode that has been used to inject current is subsequently used to measure a potential without allowing sufficient time for the charge built up at the electrode/ground interface to decay (typically a few seconds to tens of seconds). Since the CR method does not explicitly take this effect into account, its output survey designs have to be rearranged to reduce the errors that it can cause. We use a simulated annealing method that finds a near-optimal ordering to maximize the separation in time, for all the constituent commands, between electrodes being used to pass current and subsequently measure potential (Wilkinson *et al.* 2012a).

In this study, the CR method as described above was initially used to generate a static optimized survey design which would be used to monitor the controlled movement of a target in a laboratory tank, with the results being compared to those obtained from a dipole–dipole survey using the same number of multichannel commands. The measurements were made using a 10-channel automated time-lapse ERT (ALERT) system (Kuras *et al.* 2009; Ogilvy *et al.* 2009). Both the CR method and the ALERT system were subsequently modified to allow for adaptive focusing of the model resolution; these enhancements will be described later in the paper.

3 EXPERIMENTAL SETUP AND STATIC SURVEYS RESULTS

To test and compare the results of ERT monitoring using standard, static optimized and adaptive optimized surveys, we required a controlled and repeatable dynamic experimental target that could produce the same dynamic electrical resistivity structure as a function of time. To this end, we designed and constructed an
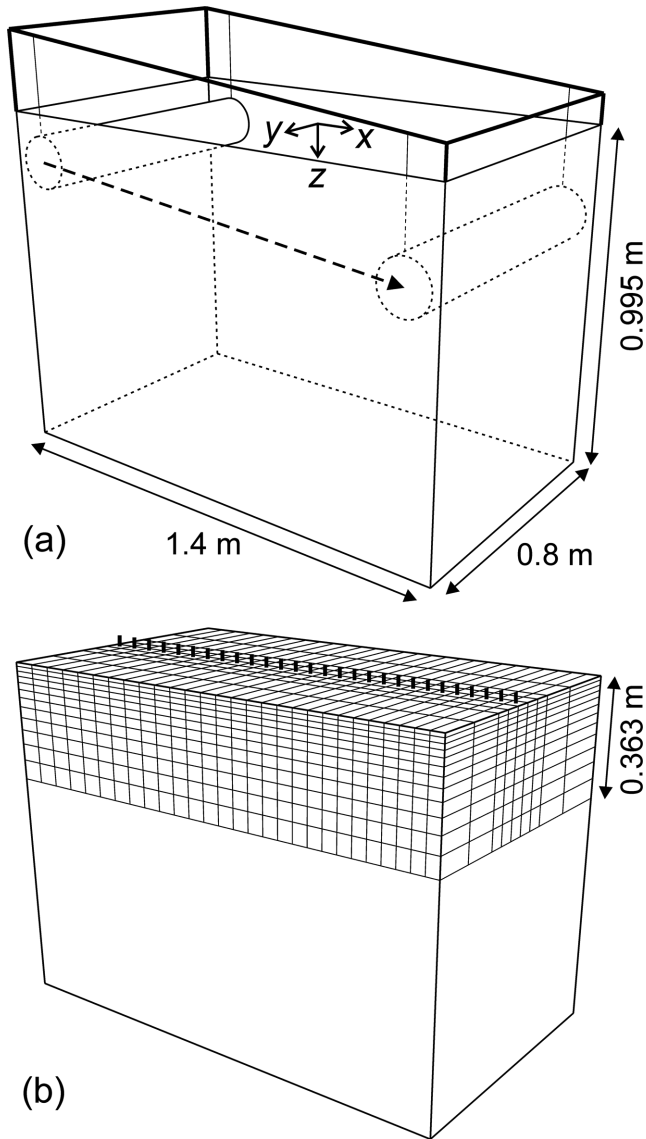
Figure 1. (a) Schematic diagram of the experiment, showing the frame, cylindrical target, path (dashed arrowed line) and tank with the dimensions of the water-filled volume. (b) Model blocks and electrode locations (bold vertical lines). Only alternate blocks are shown in the *x*- and *y*-directions for clarity.

apparatus to move an insulating cylinder through a water-filled tank along a subhorizontal path beneath and parallel to a line of surface electrodes. The tank, the target and its trajectory are shown in Fig. 1(a). The tank was 1.4 m long, 0.8 m wide and 1.0 m deep and was filled to a depth of 0.995 m with tap water. The origin of the coordinate system was taken to be in the centre of the tank in the *x*- and *y*-directions and at the water surface in the *z*-direction. The cylinder had an external diameter of 0.15 m and a length of 0.8 m and was arranged with its long axis parallel to the *y*-direction, thus extending across the full width of the tank. It was mounted 0.35 m beneath a cradle attached to a sloping ramp. The cradle was pulled down the ramp in the +*x*-direction at a constant speed by an electric motor. The cradle was also attached to counter weights suspended over pulleys at the −*x* end of the tank (not shown), with these counter weights being raised as the cradle was pulled in the +*x*-direction thereby providing resistance to the electric motor and ensuring smooth constant motion. The slope of the ramp meant that

the cylinder changed its depth beneath the surface over time, thus ensuring it passed through regions of varying sensitivity and image resolution with respect to the linear ERT electrode array. The trajectory of the centre of the cylinder was from $x = -0.600$ m, $z = 0.135$ m to $x = 0.603$ m, $z = 0.257$ m in 19 hr, giving a horizontal velocity of $dx/dt = 63$ mm hr^{-1}. The array comprised 28 electrodes, shown as short bold lines in Fig. 1(b), spaced at 0.05 m intervals symmetrically about $x = 0$ along the line $y = z = 0$. The electrodes were gold-plated 316 stainless steel rod with a diameter of 4 mm and a submerged length of 10 mm, the lower 3 mm of which formed a taper to a point. This arrangement was designed to approximate a 2.5-D ERT imaging situation in which the resistivity structure does not change in the *y*-direction. But although the ends and base of the tank could be incorporated in a 2.5-D inversion, the side walls are more difficult to accommodate. Therefore we had to use a 3-D inversion (Res3DInvX64 from Geotomo Software) that could apply suitable Neumann boundary conditions to account for the insulating walls of the tank. To account for the approximately 2-D nature of the target, the inversion was constrained so that the variation of the resistivity distribution in the *y*-direction was small compared to the *x*- and *z*-directions (Loke *et al.* 2014a). Considering the resistivity distribution as a function of *x* and *z* in the plane $y = 0$, we could then obtain an approximately 2.5-D inversion of the data despite the presence of the insulating boundaries. The distribution of model cells used in the inversion is shown in Fig. 1(b). The model extended to the full length and width of the tank in the *x*- and *y*-directions and to −0.363 m in the *z*-direction. The cell size was 0.025 m in the *x*-direction, but varied along the *y* and *z*-directions to account for the reduced sensitivity in these directions at greater distances from the electrodes. Only every other cell boundary is shown along *x* and *y* in Fig. 1(b) for clarity, although all cell boundaries are shown in the *z*-direction.

The estimated model resolution for the comprehensive set is shown in Fig. 2(a). The Jacobian matrix elements were approximated by assuming a 2.5-D homogeneous half-space. Loke *et al.* (2014a) found that the 2.5-D assumption was a suitable approximation despite the presence of the tank boundaries, and Stummer *et al.* (2004) and Wilkinson *et al.* (2012b) have shown that optimized surveys based on the sensitivity distributions of a homogeneous half-space perform very similarly to those based on heterogeneous resistivity distributions for typical numbers of measurements in an ERT data set. These findings are supported by the recent re-examination of the sensitivity function in terms of elementary signal contributions (Gómez-Treviño & Flores 2015). The damping factor in eq. (1) was $\lambda = 0.0025$ and was chosen so that the model resolution was small ($R \approx 0.05$) at the base of the image space (Wilkinson *et al.* 2012a). The static and adaptive optimized surveys studied in this paper were compared to a standard dipole–dipole survey with dipole lengths $a = 1–4$ electrode spacings and dipole separations of na, where $n = 1$ to 10. This comprised 445 four-electrode configurations and its implementation required 82 ten-channel commands. The optimized surveys were designed with the same number of commands and hence required the same amount of time and power to measure, but since the CR method can make full use of multichannel capabilities, they comprised 820 configurations. All the surveys had the same maximum geometric factor of $K_{max} = 414.7$ m, although the optimized surveys tended to have greater proportions of measurements at the high and low ends of the range of permitted *K* values (see Table 1). The relative model resolution distributions for the dipole–dipole and static optimized surveys are shown in Figs 2(b) and (c) with average relative resolutions of $S = 0.599$ and $S = 0.734$, respectively. The optimized survey gives higher resolution than the
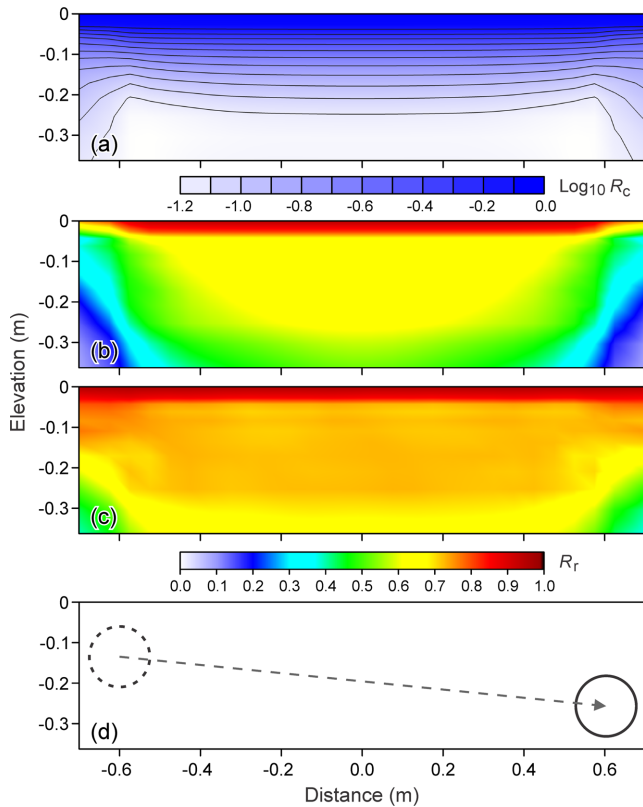
Figure 2. (a) Model resolution distribution (R_c) for the comprehensive measurement set. (b, c) Relative model resolution (R_r) distributions for the dipole–dipole and static optimized measurement sets, respectively. (d) Path of the cylindrical target (start at dashed circle, finish at solid circle). All plots shown in the $y = 0$ plane.

Table 1. Distribution of geometric factors (K) in dipole–dipole and optimized surveys.

K range (m)	Fraction of dipole–dipole survey (%)	Fraction of static optimized survey (%)	Fraction of adaptive optimized surveys (%)
0.2–0.5	0.0	2.7	1.9
0.5–1	5.6	11.5	8.4
1–2	4.9	1.6	1.8
2–5	13.3	9.1	8.2
5–10	9.7	9.3	10.6
10–20	15.3	11.2	12.3
20–50	13.0	13.9	15.2
50–100	16.6	9.0	10.7
100–200	13.7	11.8	13.8
200–500	7.9	19.9	17.1

dipole–dipole survey throughout the image space, but in particular it is significantly higher at the edges near the beginning and end of the target track, which is shown in Fig. 2(d).

The measurement time for a single survey was 23 min during which time the cylinder moved by ~24 mm. Therefore, image blurring caused by the movement of the target during measurement (Slater *et al.* 2002; Singha & Gorelick 2005; Ward *et al.* 2010; Wilkinson *et al.* 2010b; Rucker 2014) would be limited to approximately one model cell or 16 per cent of the cylinder diameter. The survey repetition frequency was one per hour in order to allow time for the system batteries to recharge. The optimized survey had been reordered to reduced electrode polarization errors, and had mini-

Table 2. Distribution of reciprocal errors in dipole–dipole and optimized data sets (without target).

Upper error (%)	Fraction of dipole–dipole survey (%)	Fraction of static optimized survey (%)
0.1	7.4	7.1
0.2	25.6	21.2
0.5	63.6	61.5
1	87.0	87.6
2	95.1	95.1
5	98.4	98.7
10	99.3	99.0
20	99.8	99.1
50	100.0	99.5

mum and average times between possible polarization effects of 1.4 and 3.4 min, respectively, which have previously been found to be sufficient to negate this source of error (Wilkinson *et al.* 2012a; Loke *et al.* 2015). Before and after each monitoring experiment, the surveys were measured in forward and reciprocal configurations to assess the levels of data noise (LaBrecque *et al.* 1996). For each configuration, the reciprocal error was calculated as the percentage standard error in the mean of the forward and reciprocal measurement (Wilkinson *et al.* 2012a). The average of the two distributions of reciprocal error is shown in Table 2 for both surveys. Data quality was excellent, and very similar for both surveys, with 98.4 per cent and 98.7 per cent of the data having reciprocal errors <5 per cent for the dipole–dipole and optimized surveys respectively.

The data were inverted with Res3DInvX64, using an L^1 data constraint and an L^2 model smoothness constraint (an L^1 model constraint was tried, but the resulting images had lower contrast and were notably affected by the underlying model grid structure). Variation of resistivity in the y-direction was damped by a factor of 10 compared to the x- and z-directions to account for the quasi-2-D nature of the target. Since noise levels were low, the inversions were performed without time-lapse constraints and directly on separate data sets, rather than on differences between subsequent sets (Miller *et al.* 2008; Wilkinson *et al.* 2010b). The mean absolute misfit errors were typically 0.6–0.8 per cent for the dipole–dipole data inversions and 0.7–0.9 per cent for the optimized data inversions. The sequences of target and inverted images are shown in Fig. 3 (only every second image is shown for conciseness). Since the target was non-conducting, the model resistivities, ρ, have been transformed into a form similar to a reflection coefficient, r, which is given by

$$r = \frac{\rho - \rho_0}{\rho + \rho_0}, \tag{3}$$

where the background resistivity of the tank water was measured to be $\rho_0 = 12.7\ \Omega$m. For perfect conductors, $r = -1$; for the background resistivity, $r = 0$; and for perfect insulators, $r = 1$. This transformation allows the inverse models to be displayed and compared quantitatively to the target. Fig. 3 demonstrates that the optimized survey design produces better images of the target than the dipole–dipole survey. In the corners of the model space where its resolution is poor, the dipole–dipole survey almost completely fails to image to the target, which is essentially absent from frames 0, 18 and 19 (19 not shown). By contrast, the target is clearly present in all frames of the optimized survey sequence. Also in the optimized images it has a greater contrast with respect to the background, and generally appears closer to circular in cross-section. A more quantitative comparison of these images is presented later in the paper along with the images from the adaptive optimization.
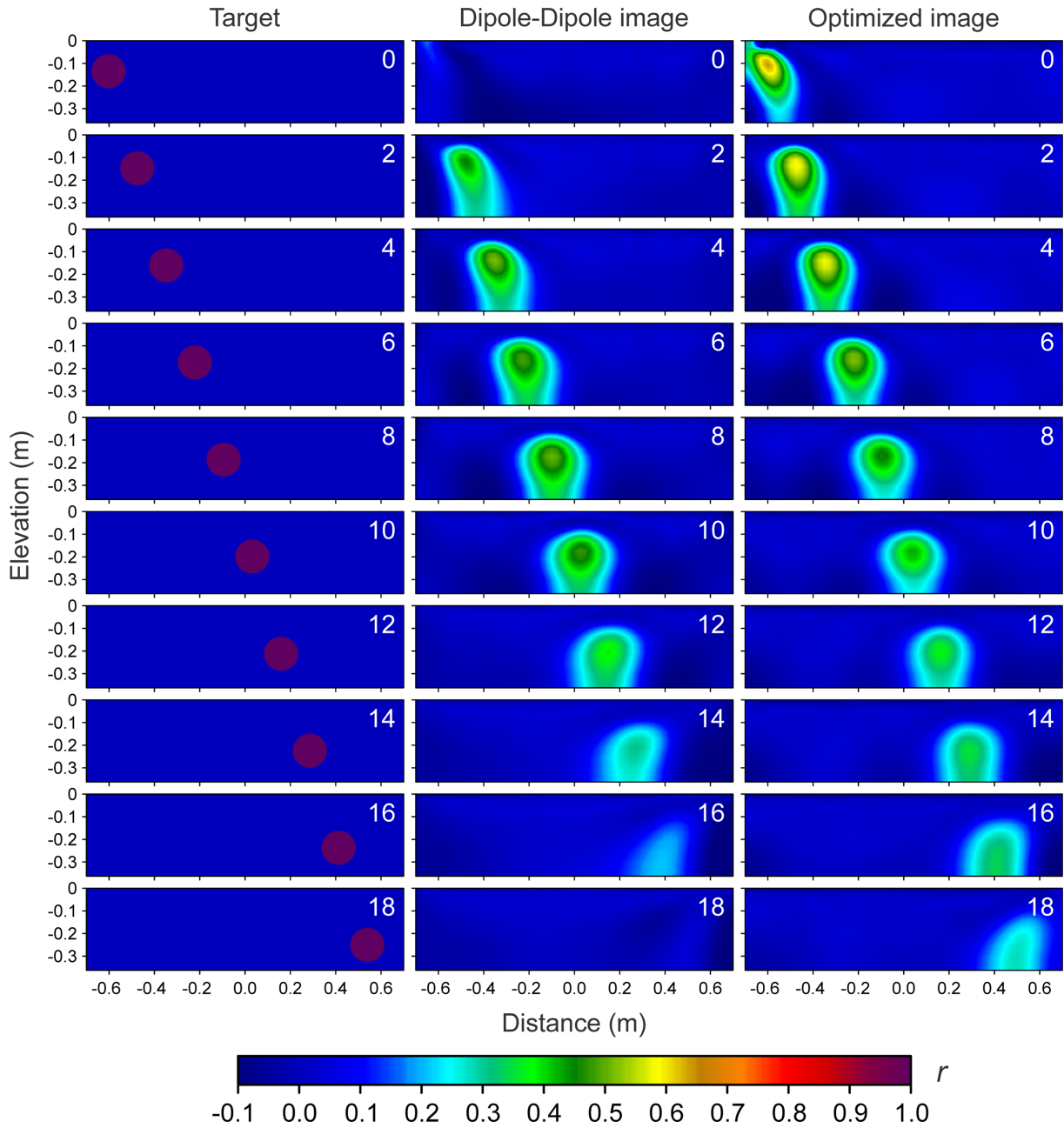
Figure 3. Target, dipole–dipole and optimized images shown in terms of reflection coefficient *r*. Values in the top right of the images show the time steps *t* of each row.

4 ADAPTIVE OPTIMIZED SURVEY DESIGN

The aim of this study is to be able to focus the design of optimized surveys for time-lapse monitoring so that they provide extra resolution in regions of the image space where changes are occurring. This requires new elements in the design algorithm that: (i) adapt, augment or redesign an optimized survey; (ii) identify regions of interest from previous results; and (iii) enhance the model resolution within these regions. The majority of optimal design applications in geophysics have used local or 'greedy' design algorithms, which iteratively make locally optimal changes to a survey design until some pre-determined stopping criterion is reached (Curtis *et al.* 2004; Stummer *et al.* 2004; Wilkinson *et al.* 2006, 2012a; Coles & Morgan 2009; Guest & Curtis 2009). These iterative methods

are not guaranteed to be globally optimal but they tend to produce high-quality results and are much faster than global methods (Coles & Curtis 2011), which are only practical in cases where the problem is described by a small number of model parameters (Ajo-Franklin 2009; Roux & Garcia 2014). Since iterative locally optimal methods can proceed by construction, decimation or exchange of measurement configurations (Coles & Prange 2012), our first new requirement, that of adapting surveys over time, should be straightforward in principle. By removing a number of measurements found to be less optimal in light of previous experimental results and replacing them with more optimal choices, the survey could be redesigned to any desired degree. However, the multichannel structure of the surveys makes this rather difficult in practice, especially if only a small fraction of the survey is to be replaced.
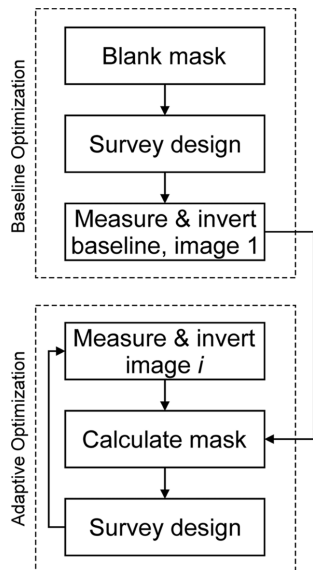
Figure 4. Flow chart showing the operation of the adaptive optimization algorithm.

Figure 5. Relative frequency distribution of the background variations Δ in the static optimized monitoring images. The dashed line shows a normal distribution with the same standard deviation and zero mean, the solid line shows the equivalent Laplace distribution.

This is because the existing remaining measurements greatly limit the choice of replacements. For example, in an M-channel system, an exchange algorithm, where measurements are replaced individually, would only be able to change the two measurements at the ends of the command; the centre $M - 2$ measurements would be fixed by the other configurations. Even the choice for replacing the end configurations would be extremely limited (both current electrodes and one potential electrode would be fixed in each case). A possibility might be to use an exchange algorithm on commands rather than measurements, but this would risk removing still-optimal measurements as well as less beneficial ones. Due to these limitations, and the availability of efficient implementations of the CR method that have recently been developed (Loke *et al.* 2010a,b, 2015), we chose instead to design a new survey by construction at each step of the experiment.

The second new requirement was to identify regions of interest from previous ERT monitoring images. Our design algorithm uses a binary 'change mask' to identify whether or not a cell requires extra resolution to be focused on it in the next survey. Since our experiment involved tracking a target, we chose to determine the change mask by comparing the preceding image to an initial baseline that was obtained before the target was placed in the tank. The flowchart in Fig. 4 describes the operation of the algorithm. Initially no focusing is used (i.e. a 'blank mask'), which produces the same survey as the standard CR method in the previous section. This survey is then carried out, and the data are inverted to form the baseline image. The same survey design is also used to obtain the data set at the first time step with the target present. Once the first image of the target is available, the changes between it and the baseline image are used in the calculation of the next change mask. This is then used to design the survey for the second time step and the process is iterated, with surveys at subsequent time steps being designed using masks generated by comparing the image at the preceding time step to the baseline image.

A wide variety of methods are available to detect changes in time-lapse images (İlsever & Ünsalan 2012). We have adopted and modified a block-based significance test that examines changes in a block of n_b cells surrounding and including the cell being tested (Radke *et al.* 2005). The null (no-change) hypothesis is that the
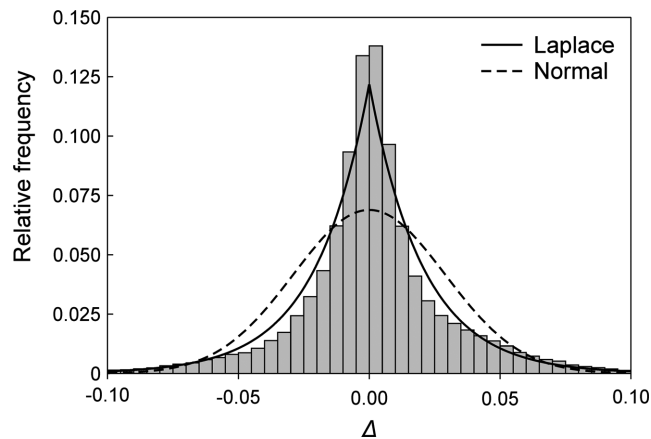
differences between images are the results of noise in the data. Typically the cell differences Δ_i in a block are assumed to be independent and identically distributed (iid), and are often modelled as being normally distributed with mean $\mu = 0$ and variance σ^2. In this case the test statistic

$$g_{\chi^2} = \sum_{i=1}^{n_b} \frac{\Delta_i^2}{\sigma^2} \tag{4}$$

has a χ^2 probability density function with n_b degrees of freedom, and so a standard χ^2 significance test is applied to determine whether or not the observed differences are consistent with the null hypothesis given the expected degree of background variation in the images (Radke *et al.* 2005).

The distribution of background variations in the images was determined by examining the unchanged regions of the images obtained by static optimized monitoring in the preceding section. The differences were taken between the logarithms of the cell resistivities, that is between images 0 and 1 the difference of the ith cell was $\Delta_i = \log_{10}(\rho_{1i}) - \log_{10}(\rho_{0i})$. The results are shown in the histogram in Fig. 5. They were obtained by examining the changes in background regions between all possible pairs of images. We set a limit of $|r| \leq 0.11$ in both images of a given pair to specify the background regions (i.e. those regions uninfluenced by the target in both images). Although the results did not depend strongly on the chosen limit, if it was much smaller, the distribution became clearly truncated at larger $|\Delta|$. Conversely if it was much larger, the distribution became distorted by large Δ values caused by the presence of the target. The distribution has $\mu = 0.001$, $\sigma = 0.029$ and a low skewness of 0.013. Fig. 5 also shows the continuous relative frequencies for a normal distribution with $\mu = 0$ and $\sigma = 0.029$ and a Laplace distribution with $\mu = 0$ and shape parameter $\beta = \sigma/\sqrt{2} = 0.021$. It is clear that the Laplace distribution is a better model for the distribution of background variations in these images, which is more strongly peaked and has longer tails than a normal distribution. Therefore we modelled the cell differences as iid Laplacian random variables. In this case, under the null hypothesis the test statistic for a block of n_b cells

$$g_{\Gamma} = \sum_{i=1}^{n_b} \frac{|\Delta_i|}{\sigma} \tag{5}$$
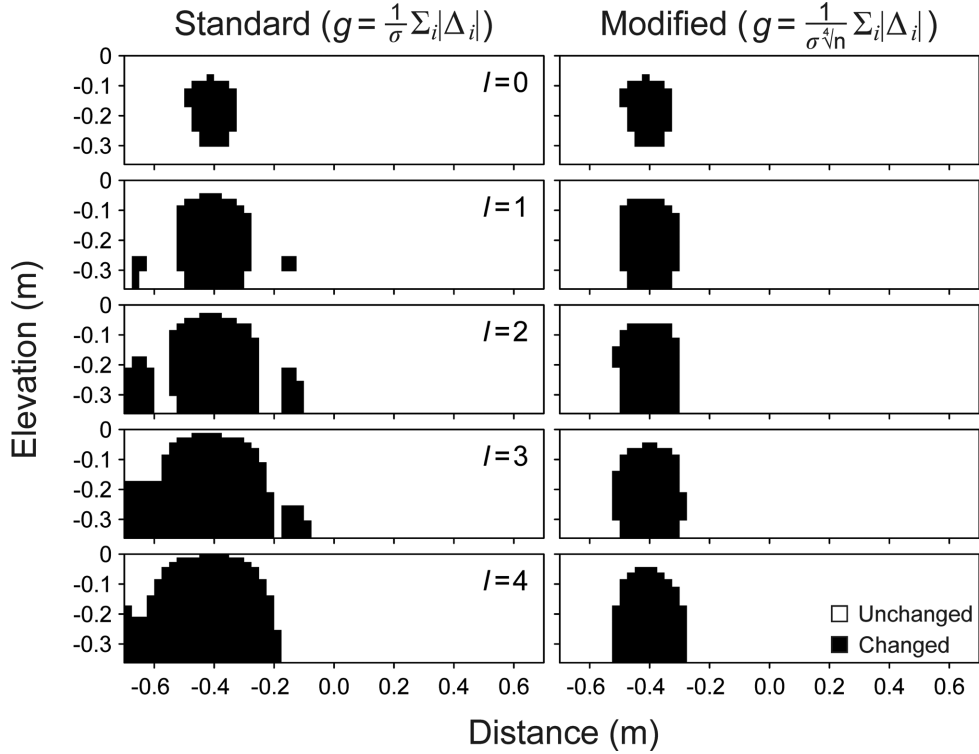
Figure 6. Change masks calculated for blocks of side lengths $2l + 1$. Left-hand column shows the results using the standard test statistic. Right-hand column shows the results using the modified test statistic to reduce the effect of correlations in the smoothness-constrained inversions.

has a probability density function given by a Γ distribution with shape parameter n_b and scale parameter $1/\sqrt{2}$ (Kotz *et al.* 2001). If the null hypothesis was rejected at the chosen significance level then the changes of the cells in the block were deemed to be significant and the change mask was set to one for the centre cell, otherwise it was set to zero. Applying the block result to the centre cell only, rather than the whole block, requires the use of overlapping blocks and more calculations, but typically produces better results than using non-overlapping blocks (Radke *et al.* 2005). The significance level for the Γ distribution test was set to 0.001. Since there were 672 cells in each image this meant that, on average, fewer than one cell per image would be misidentified.

The assumption that the cell variations are iid is rarely strictly valid in image change detection (Radke *et al.* 2005) and in smoothness-constrained geophysical imaging, correlations between nearby cells are actually imposed by the inversion algorithm (Loke *et al.* 2003). Under the iid assumption, using larger blocks of cells in the change detection process should increase the smoothness of the change mask but should not significantly change the number of cells identified as having changed (Radke *et al.* 2005). But due to the correlations in the smoothness-constrained images, we found that the null hypothesis was rejected for greater numbers of cells as the block size increased. The left-hand column of Fig. 6 shows change masks calculated for the same image/baseline pair with different block sizes, where the block had side lengths of $2l + 1$. To try to counteract the effects of correlation, we divided the test statistic in eq. (5) by the fourth root of the number of cells in the block, that is,

$$g_\Gamma = \sum_{i=1}^{n_b} \frac{|\Delta_i|}{\sigma \sqrt[4]{n_b}}. \tag{6}$$

This change was entirely empirically motivated and informed, but seemed to maintain the approximate size of the changed regions with increasing block size (right-hand column in Fig. 6). A block size of $l = 1$ was chosen for use in the adaptive optimized imaging experiment.

The final new element in the adaptive design algorithm is a method for focusing the model resolution to enhance it in the changed regions. Previous methods used to increase resolution or sensitivity, or similarly to reduce uncertainty, within a target region include: removing the untargeted regions of the image from the optimization process (Stummer *et al.* 2004; Nenna *et al.* 2011); forming a least-squares fit of sensitivity distributions to a desired focused sensitivity pattern (Hennig *et al.* 2008); and adjusting the prior model covariance in the target region (Khodja *et al.* 2010; Djikpesse *et al.* 2012). Here we changed the average relative resolution maximized by the CR method, eq. (2), to a weighted average

$$S = \frac{1}{m} \sum_{j=1}^{m} \frac{w_j R_j}{R_{cj}} \tag{7}$$

where w_j is the weight of the jth cell. This allowed each cell to have a different weight in the sum, enabling the model resolution to be focused on regions of interest. An example of a baseline image, a target image, its change mask, and the resulting focused survey model resolution are shown in Figs 7(a)–(d), respectively. It is clear by comparing Fig. 7(d) to Fig. 2(c) that there is an enhancement of relative model resolution in the vicinity of the changed region associated with the target, albeit at the expense of a decrease in resolution in other parts of the image. But it is worth noting that the reduced resolution outside of the region of interest is still everywhere greater than or equal to the resolution provided by the standard dipole–dipole survey (Fig. 2b). So even though the image
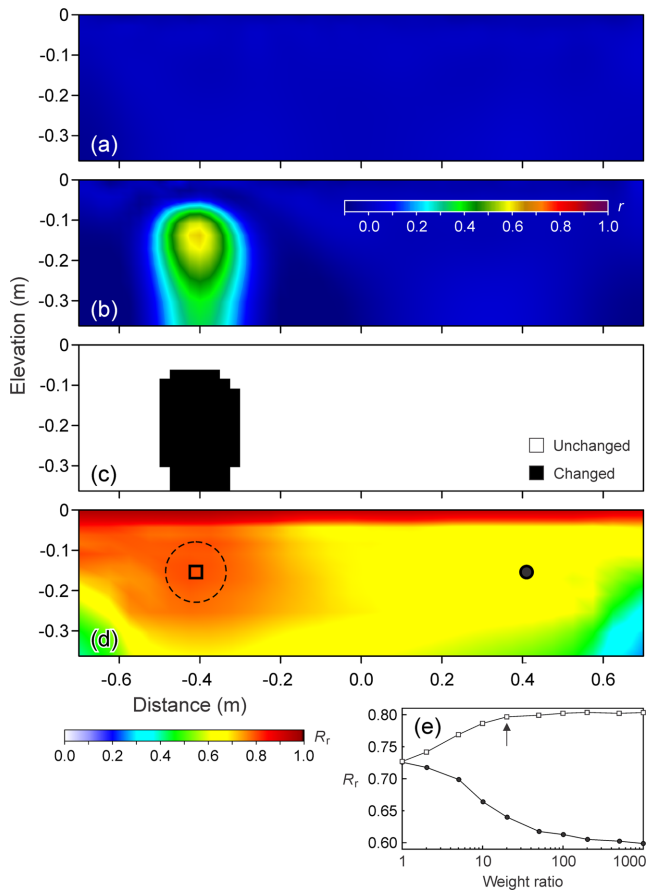
Figure 7. Example of focused survey design. (a) Baseline image. (b) Previous image. (c) Resulting change mask. (d) Relative model resolution R_r of targeted survey, with highlighting of the target (dashed circle), centre of the target (open square) and symmetric point about the electrode array centre (filled circle). (e) Relative model resolution at the target centre (open squares) and symmetric point (filled circles) as functions of the weighting ratio of changed and unchanged cells.

resolution is now more strongly focused within the region of interest, if new changes were to occur outside this region they would still be imaged at least as well as by a dipole–dipole survey. These new changes would then form part of the subsequent region of interest that would be focused upon in the next iteration. The focused survey designs used in this paper were obtained by setting $w_c = 1$ for changed cells and $w_u = 0.05$ for unchanged cells. The weight for the unchanged cells was determined by examining the relative model resolution at the centre of the target (indicated by the open square within the dashed line in Fig. 7d) and at the symmetric point about $x = 0$ (filled circle) as a function of the ratio w_c/w_u (see Fig. 7e). Without weighting (ratio = 1), the resolutions at both points are approximately equal. At greater ratios, the resolution increases in the target region and decreases outside. At a ratio of 20 ($w_u = 0.05$), the resolution within the target is close to maximal (arrowed in Fig. 7e) but the resolution outside the target is still decreasing. Therefore we chose $w_u = 0.05$ since reducing this further did little to improve the resolution of the target, but adversely affected the resolution in the rest of the image space.

To implement the adaptive optimization algorithm, we modified the control software of the ALERT system to allow it to change the stored survey command sequences dynamically. In the standard system, measurement schedules are typically defined by the user ahead of a monitoring sequence. For the adaptive system, the

control software was changed so that it regularly examined a local 'drop' folder for the presence of a modified command file. If one was found before the next measurement set was scheduled, it would be uploaded to the ALERT system to replace the existing command sequence. Therefore the adaptive monitoring sequence was realized by setting up a regular monitoring schedule using a given command sequence identifier. Immediately after each scheduled set of measurements, which took 23 min to acquire, the most recent data set would be inverted and a new focused optimized survey would be designed based on the changes between the image of the target and the baseline. This survey would then be reordered to avoid polarization errors. The process of data inversion, survey optimization and reordering took 22 min on average. The new survey would be given the same identifier as the command sequence to be replaced on the system and placed in the drop folder. The control software would then upload the new command sequence to the system before the next measurement set was scheduled to begin.

5 ADAPTIVE SURVEY RESULTS

The adaptive optimization algorithm and modified ALERT system were tested by repeating the target monitoring experiment. The parameters for the experiment were identical to those used previously, with the exception of the background resistivity of the tank water which was measured to be $\rho_0 = 14.0$ Ωm. Two extra data sets were measured before the main monitoring sequence. The first was to establish the baseline image and was measured with no target in the tank (the row labelled 'Base' in Fig. 8). It used a blank change mask to generate the survey, which was therefore identical to the static optimized survey used previously. After the target was inserted at the far left hand edge of the tank, the same blank mask survey was repeated to generate the first image of the target (the row labelled 'Pre' in Fig. 8). The 'Pre' image was used to generate the initial change mask of the monitoring sequence (labelled '0'). The adaptive monitoring was then performed for 20 time steps, where data at the ith time step was measured using a survey design based on the mask created from the changes between image$_{i-1}$ and image$_{base}$, that is, repeated iteration of the sequence: (image$_{i-1}$ − image$_{base}$) → mask$_i$ → survey$_i$ → image$_i$. Fig. 8 shows the change masks, adaptive survey relative resolution plots and images of the target resulting from the monitoring sequence (note that only even numbered steps are shown). The images at steps 0 to 18 are directly comparable with the identically numbered dipole–dipole and static optimized images shown in Fig. 3. The time intervals between images were identical to those in the previous experiments, with the adaptive optimization processing required to generate the next survey being carried out while the system batteries were recharging. The mean absolute misfit errors were typically 0.8–1.0 per cent for the adaptive optimized surveys, compared to 0.7–0.9 per cent for the static optimized and 0.6–0.8 per cent for the dipole–dipole surveys. It is not immediately clear why the adaptive optimized survey misfits were slightly higher than the static optimized misfits. The geometric factors (Table 1) were smallest on average for the dipole–dipole surveys ($\overline{K}_{DD} = 58.0$ m), which have the lowest noise levels as would be expected. However, the geometric factors were on average slightly lower for the adaptive optimized surveys ($\overline{K}_{ADP} = 84.9$ m) than the static optimized surveys ($\overline{K}_{OPT} = 89.1$ m), so this cannot explain the observed slight increase in noise levels. Although no reciprocal measurements were performed for the adaptive surveys, we suspect that the ambient noise levels must have been higher than in the earlier experiments, which were performed over a month
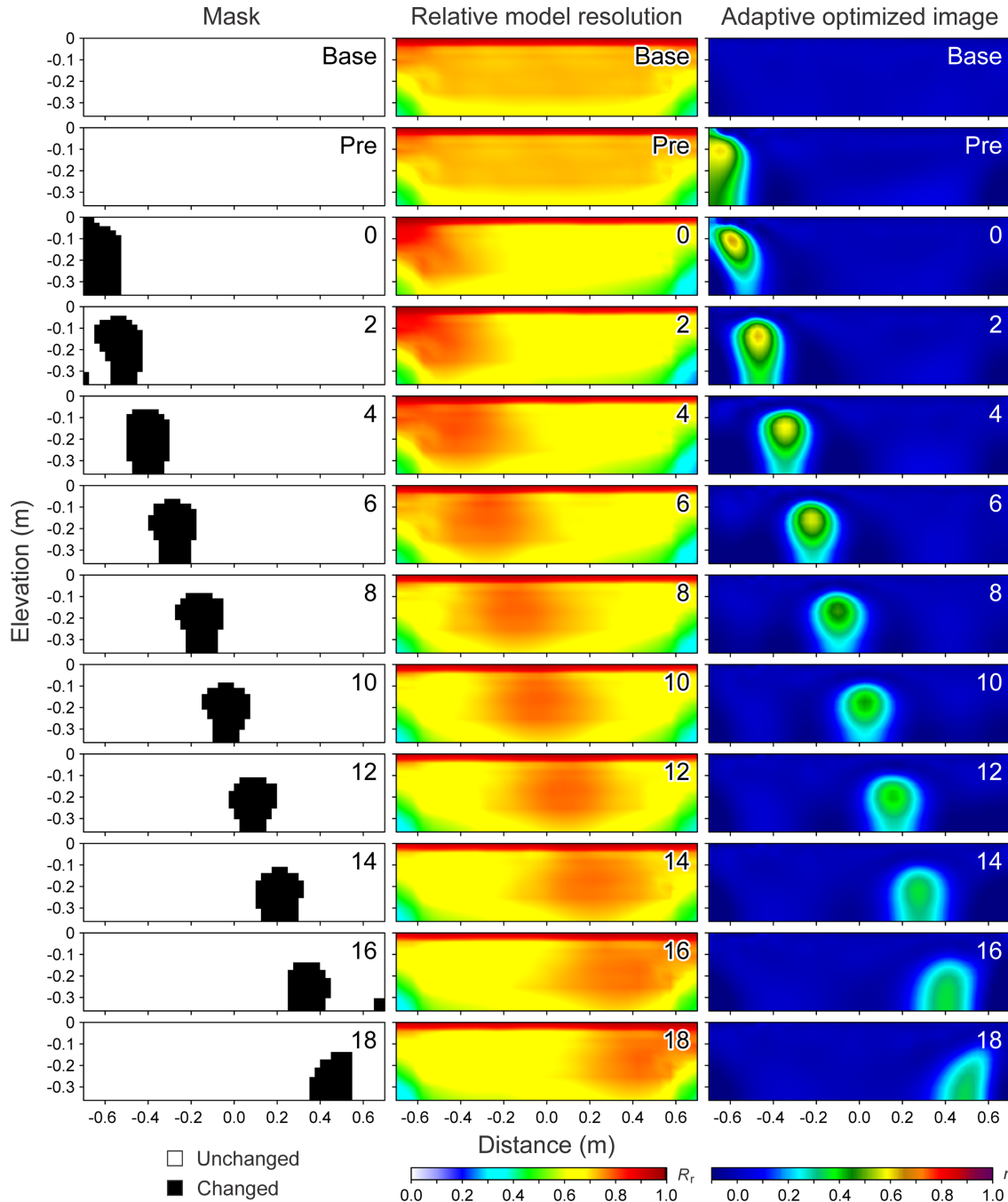
Figure 8. Change masks, relative model resolution distributions (R_r), and adaptive optimized images shown in terms of reflection coefficient r. Values in the top right of the plots show the time steps t of each row. 'Base' and 'Pre' indicate baseline and pre-experiment conditions, respectively.

before. This is supported by the measurements of the median stacking error provided by the ALERT system, which had an average of 0.019 per cent across the whole dipole–dipole monitoring experiment, 0.026 per cent for the static optimized experiment, and 0.033 per cent for the adaptive optimized experiment.

6 COMPARISON OF RESULTS AND DISCUSSION

Qualitatively the adaptive optimized images (Fig. 8) are similar to the static optimized images (Fig. 3), but the target tends to have slightly higher contrast (greater maximum r values) and be

more tightly localized. To provide a more quantitative assessment, Fig. 9 shows two measures of image quality (the Pearson correlation coefficient and the RMS difference) for comparisons between the actual target (discretized onto the same model grid) and the dipole–dipole, static optimized and adaptive optimized images. As expected, the image resolution decreases with time as the depth of the target increases. It is also clear that both types of optimized survey monitoring produced images that more accurately matched the target than the dipole–dipole images (i.e. they have greater correlation coefficients and lower RMS differences). Over the 20 time-steps, the average increase in the correlation coefficient between the dipole–dipole and static optimized images was 0.125, and the average decrease in RMS difference was 0.0117. The average extra
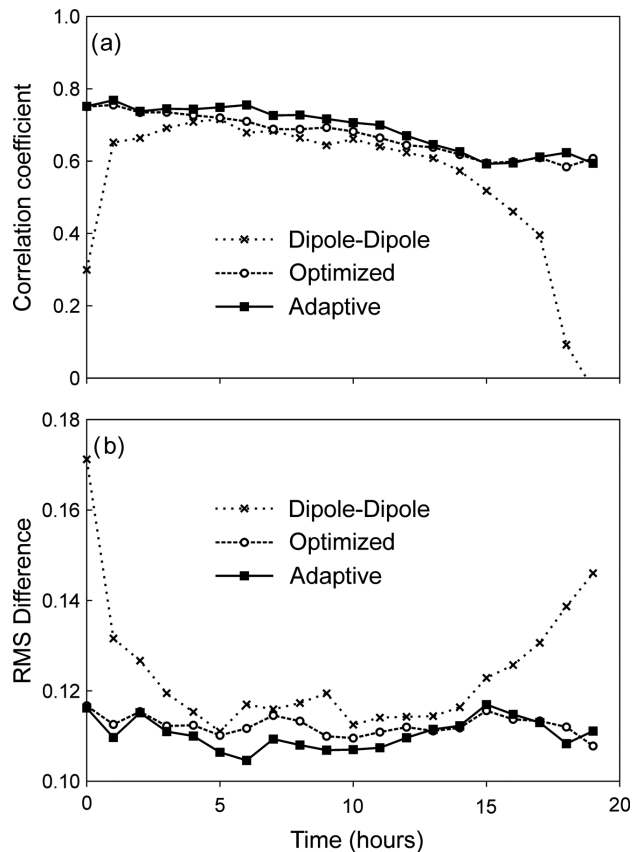
Figure 9. (a) Correlation coefficients plotted as a function of time between the target and the dipole–dipole, static optimized and adaptive optimize images. (b) RMS differences plotted similarly.

correlation increase gained by using adaptive optimization, that is, the increase between the static and adaptive optimized images, was 0.017, an improvement of 14 per cent. Similarly, the average extra decrease in the RMS difference was 0.0019, an improvement of 16 per cent.

Although the example presented here was simple, with a well-defined target geometry in a low-noise laboratory environment, the results ought to be applicable to most resistivity monitoring field applications, providing that the data can be inverted and the survey design can be calculated quickly enough. To avoid aliasing, it is desirable for the period between monitoring surveys to be at most half of the characteristic timescales of the processes being monitored (the Nyquist limit, Rucker 2014). Data acquisition will require some fraction of this monitoring interval, so inversion, survey design and command reordering must take place within the remaining time. Of these tasks, the time taken for survey design has the most unfavourable scaling with the size of the investigation. If the monitoring involves N electrodes, n measurement configurations (n is approximately proportional to N) and m model cells (m is approximately proportional to $N \log(N)$), survey design time varies approximately as $N^2 m^2 \log(n)$, compared to n^2 for reordering, and mn for inversion (Wilkinson *et al.* 2012a; Loke *et al.* 2015). Survey designs for electrode arrays with a large number of electrodes (e.g. 120) can be calculated on an ordinary personal computer in less than an hour, and for very large numbers of electrodes (e.g. 200) in under a day (Loke *et al.* 2015). Since it is likely that ERT monitoring in the field will have periods of at least hours (Ward *et al.* 2010; Wilkinson *et al.* 2010b), adaptive optimization should be possible in most circumstances.
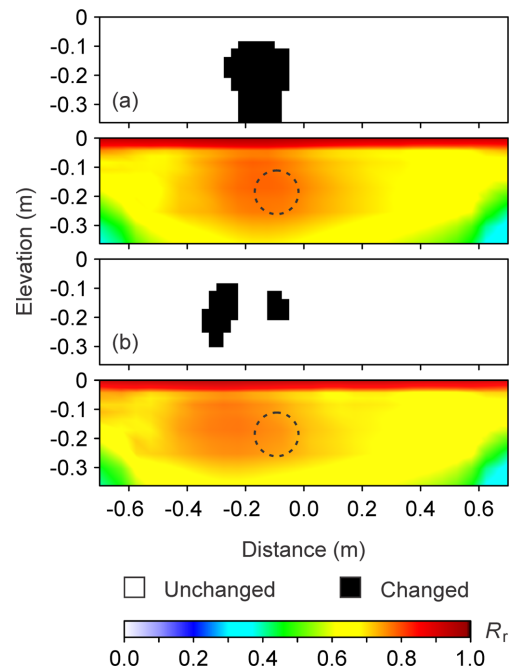

Figure 10. (a) Example of a change mask and resulting survey relative model resolution (R_r) distribution calculated relative to the baseline image. (b) Change mask and R_r distribution calculated relative to the preceding image.

A further issue with field applications could be the lack of a baseline image representing the monitoring region in a quiescent or background state. In these cases, it would be possible to use differences between the previous two images (at $t-1$ and $t-2$) to define the change mask, rather than differences between the previous image ($t-1$) and the baseline (t_B). This is demonstrated in Fig. 10, which compares the change masks and associated survey resolution distributions calculated at $t = 8$ hr with respect to either t_B or $t-2$. The surveys would be used to generate an image of the target at the location shown by the dashed circles. If a baseline is not used, the focal location depends on information from $t-2$ as well as from $t-1$, which causes the resulting resolution distribution to be focused further back along the target track than if the baseline is used (Fig. 10). The approximation inherent in the adaptive optimization scheme that the focus of the next survey should be defined by regions of significant change in previous images might therefore be less valid if a baseline cannot be defined. But since the focal region is not as tightly defined as the target, due to the smoothness constrained inversion and the spatially distributed sensitivities of the measurements, the target still lies in the enhanced region even if the two preceding images are used to define it. An interesting possibility for future research would be to incorporate forward prediction into the change mask calculation, so that the focus on dynamic regions of change could be more accurately estimated. This might be done using Kalman filters (Kim *et al.* 2005; Lehikoinen *et al.* 2009) or hydrogeophysical modelling (Kemna *et al.* 2002; Singha *et al.* 2008; Pollock & Cirpka 2010; Kowalsky *et al.* 2011; Doetsch *et al.* 2012).

Although noise levels were low enough in this study that a simple maximum geometric factor provided a sufficient design constraint in the optimization process (Wilkinson *et al.* 2012a), this would not necessarily be true in field applications. If noise levels are significant compared to modelling errors, then the data covariance matrix can be weighted appropriately in the survey design (Blome *et al.* 2011; Wilkinson *et al.* 2012a). If the noise levels vary

significantly during the monitoring experiment, and if they could be estimated from the data, then the data covariance matrix could be updated with time instead of, or as well as, the change mask. This would allow for adaptive design with respect to changes in noise conditions and/or regions of interest. When resistivity data are noisy, it is also desirable to apply more sophisticated time-lapse strategies than simple separate inversion as used here (Miller *et al.* 2008). Although difference inversion would not be applicable (since the measurements used in successive surveys are not the same), 4-D inversion with time-lapse constraints (Kim *et al.* 2009; Karaoulis *et al.* 2011; Loke *et al.* 2014c) would be able to handle time-dependent survey configurations. An interesting possibility would be to use the change mask to define the amount of variation allowed in different regions of the time-lapse inversion (Karaoulis *et al.* 2014) as well as to focus the model resolution.

7 CONCLUSIONS

We have used a well-controlled repeatable laboratory experiment to provide a proof-of-concept demonstration of using time-lapse adaptive optimized survey design to improve image quality in geoelectrical monitoring experiments. The adaptive optimization algorithms were based on proven methods to generate static optimized surveys, which can also be used for enhanced geoelectrical monitoring, but which do not change over time. They were implemented using an existing automated geoelectrical imaging system and a standard personal computer. The algorithms could be executed during the normal measurement and recharge cycle of the monitoring system, and took no more power or time than either standard dipole–dipole or static optimized survey designs.

The experiment involved imaging a cylindrical target moving at constant velocity along a subhorizontal path beneath a linear array of electrodes. The target was imaged using dipole–dipole, static optimized and adaptive optimized surveys. The static optimized surveys produced quantitatively superior images to the dipole–dipole data. The adaptive optimization gave an extra 14–16 per cent increase in image quality compared to the static optimized images, depending on the measure used. Although this experiment was a small-scale example with low noise levels and a well-defined target geometry, optimized survey design for resistivity monitoring is practical for field installations with an order-of-magnitude more electrodes and can account for data noise and the lack of clean baselines. In general, the algorithms presented here ought to be applicable to most resistivity monitoring experiments provided that the data can be inverted and the survey design can be calculated in less time than the data acquisition interval (i.e. more quickly than the characteristic timescales of the processes being monitored).

ACKNOWLEDGEMENTS

REFERENCES

Ajo-Franklin, J.B., 2009. Optimal experiment design for time-lapse travel-time tomography, *Geophysics,* **74,** Q27–Q40.

Alaeddini, A., Yang, K. & Murat, A., 2013. ASRSM: a sequential experimental design for response surface optimization, *Qual. Reliab. Eng. Int.,* **29,** 241–258.

Blome, M., Maurer, H. & Greenhalgh, S., 2011. Geoelectric experimental design – efficient acquisition and exploitation of complete pole-bipole data sets, *Geophysics,* **76,** F15–F26.

Chambers, J.E. *et al.*, 2014. 4D electrical resistivity tomography monitoring of soil moisture dynamics in an operational railway embankment, *Near Surf. Geophys.,* **12,** 61–72.

Coles, D.A. & Morgan, F.D., 2009. A method of fast, sequential experimental design for linearized geophysical inverse problems, *Geophys. J. Int.,* **178,** 145–158.

Coles, D. & Curtis, A., 2011. Efficient nonlinear Bayesian survey design using DN-optimization, *Geophysics,* **76,** Q1–Q8.

Coles, D. & Prange, M., 2012. Toward efficient computation of the expected relative entropy for nonlinear experimental design, *Inverse Probl.,* **28,** doi:10.1088/0266-5611/28/5/055019.

Coscia, I., Greenhalgh, S.A., Linde, N., Doetsch, J., Marescot, L., Gunther, T., Vogt, T. & Green, A.G., 2011. 3D crosshole ERT for aquifer characterization and monitoring of infiltrating river water, *Geophysics,* **76,** G49–G59.

Curtis, A., Michelini, A., Leslie, D. & Lomax, A., 2004. A deterministic algorithm for experimental design applied to tomographic and microseismic monitoring surveys, *Geophys. J. Int.,* **157,** 595–606.

Dahlin, T., 2000. Short note on electrode charge-up effects in DC resistivity data acquisition using multi-electrode arrays, *Geophys. Prospect.,* **48,** 181–187.

de Bruin, S., Ballari, D. & Bregt, A.K., 2012. Where and when should sensors move? Sampling using the expected value of information, *Sensors,* **12,** 16 274–16 290.

Djikpesse, H.A., Khodja, M.R., Prange, M.D., Duchenne, S. & Menkiti, H., 2012. Bayesian survey design to optimize resolution in waveform inversion, *Geophysics,* **77,** R81–R93.

Doetsch, J., Linde, N., Vogt, T., Binley, A. & Green, A.G., 2012. Imaging and quantifying salt-tracer transport in a riparian groundwater system by means of 3D ERT monitoring, *Geophysics,* **77,** B207–B218.

Franceschini, G. & Macchietto, S., 2008. Model-based design of experiments for parameter precision: state of the art, *Chem. Eng. Sci.,* **63,** 4846–4872.

Gómez-Treviño, E. & Flores, C., 2015. Alternative theory for signal contribution sections and depth of investigation characteristics in electrical prospecting, *Geophys. Prospect.,* **63,** 740–749.

Guest, T. & Curtis, A., 2009. Iteratively constructive sequential design of experiments and surveys with nonlinear parameter-data relationships, *J. geophys. Res.,* **114,** B04307, doi:10.1029/2008JB005948.

Hennig, T., Weller, A. & Möller, M., 2008. Object orientated focussing of geoelectrical multielectrode measurements, *J. appl. Geophys.,* **65,** 57–64.

Hilbich, C., Fuss, C. & Hauck, C., 2011. Automated time-lapse ERT for improved process analysis and monitoring of frozen ground, *Permafrost and Periglacial Processes,* **22,** 306–319.

İlsever, M. & Ünsalan, C., 2012. *Two-Dimensional Change Detection Methods,* Springer.

Karaoulis, M., Tsourlos, P.I., Kim, J.-H. & Revil, A., 2014. 4D time-lapse ERT inversion: introducing combined time and space constraints, *Near Surf. Geophys.,* **12,** 25–34.

Karaoulis, M.C., Kim, J.-H. & Tsourlos, P.I., 2011. 4D active time constrained resistivity inversion, *J. appl. Geophys.,* **73,** 25–34.

Kemna, A., Vanderborght, J., Kulessa, B. & Vereecken, H., 2002. Imaging and characterisation of subsurface solute transport using electrical resistivity tomography (ERT) and equivalent transport models, *J. Hydrol.,* **267,** 125–146.

Khodja, M.R., Prange, M.D. & Djikpesse, H.A., 2010. Guided Bayesian optimal experimental design, *Inverse Probl.,* **26,** doi:10.1088/0266-5611/26/5/055008.

Kiessling, D., Schmidt-Hattenberger, C., Schuett, H., Schilling, F., Krueger, K., Schoebel, B., Danckwardt, E., Kummerow, J. & CO$_2$SINK Group, 2010. Geoelectrical methods for monitoring geological CO$_2$ storage: first results from cross-hole and surface-downhole measurements from the

CO$_2$SINK test site at Ketzin (Germany), *International Journal of Greenhouse Gas Control,* **4,** 816–826.

Kim, K.Y, Kim, S.B., Kim, M.C., Lee, K.J., Ko, Y.J. & Kim, S., 2005. Electrical impedance imaging of two-phase flows undergoing rapid transient: Part I. Dynamic imaging, *Int. Commun. Heat Mass Transfer,* **32,** 639–647.

Kim, J.H., Yi, M.J., Park, S.G. & Kim, J.G., 2009. 4-D inversion of DC resistivity monitoring data acquired over a dynamically changing earth model, *J. appl. Geophys.,* **68,** 522–532.

Kotz, S., Kozubowski, T.J. & Podgórski, K., 2001. *The Laplace Distribution and Generalizations,* Springer Science + Business Media.

Kowalsky, M.B., Gasperikova, E., Finsterle, S., Watson, D., Baker, G. & Hubbard, S.S., 2011. Coupled modeling of hydrogeochemical and electrical resistivity data for exploring the impact of recharge on subsurface contamination, *Water Resour. Res.,* **47,** W05209, doi:10.1029/2009WR008947.

Kuras, O., Pritchard, J.D., Meldrum, P.I., Chambers, J.E., Wilkinson, P.B., Ogilvy, R.D. & Wealthall, G.P., 2009. Monitoring hydraulic processes with automated time-lapse electrical resistivity tomography (ALERT), *C. R. Geoscience, 341,* 868–885.

LaBrecque, D.J., Miletto, M., Daily, W., Ramirex, A. & Owen, E., 1996. The effects of noise on Occam's inversion of resistivity tomography data, *Geophysics,* **61,** 538–548.

Lehikoinen, A., Finsterle, S., Voutilainen, A., Kowalsky, M.B. & Kaipio, J.P., 2009. Dynamical inversion of geophysical ERT data: state estimation in the vadose zone, *Inverse Problems in Science and Engineering,* **17,** 715–736.

Loke, M.H., Acworth, I. & Dahlin, T., 2003. A comparison of smooth and blocky inversion methods in 2D electrical imaging surveys, *Explor. Geophys.,* **34,** 182–187.

Loke, M.H., Wilkinson, P.B. & Chambers, J.E., 2010a. Fast computation of optimized electrode arrays for 2D resistivity surveys, *Comput. Geosci.,* **36,** 1414–1426.

Loke, M.H., Wilkinson, P.B. & Chambers, J.E., 2010b. Parallel computation of optimized arrays for 2-D electrical imaging surveys, *Geophys. J. Int.,* **183,** 1302–1315.

Loke, M.H., Wilkinson, P.B., Chambers, J.E. & Strutt, M., 2014a. Optimized arrays for 2D cross-borehole electrical tomography surveys, *Geophys. Prospect.,* **62,** 172–189.

Loke, M.H., Wilkinson, P.B., Uhlemann, S.S, Chambers, J.E. & Oxby, L.S., 2014b. Computation of optimized arrays for 3-D electrical imaging surveys, *Geophys. J. Int.,* **199,** 1751–1764.

Loke, M.H., Dahlin, T. & Rucker, D.F., 2014c. Smoothness-constrained time-lapse inversion of data from 3D resistivity surveys, *Near Surf. Geophys.,* **12,** 5–24.

Loke, M.H., Wilkinson, P.B., Chambers, J.E., Uhlemann, S.S. & Sorensen, J.P.R., 2015. Optimized arrays for 2-D resistivity survey lines with a large number of electrodes, *J. appl. Geophys.,* **112,** 136–146.

Maurer, H.R., Boerner, D.E. & Curtis, A., 2000. Design strategies for electromagnetic geophysical surveys, *Inverse Probl.,* **16,** 1097–1118,

Maurer, H., Curtis, A. & Boerner, D.E., 2010. Recent advances in optimized geophysical survey design, *Geophysics,* **75,** 75A177–75A194.

Menke, W., 1989. *Geophysical Data Analysis: Discrete Inverse Theory,* Rev. edn., Academic Press.

Merriam, J.B., 2005. Injection electrode overprinting, *J. Environ. Eng. Geophys.,* **10,** 365–370.

Miller, C.R., Routh, P.S., Brosten, T.R. & McNamare, J.P., 2008. Application of time-lapse ERT imaging to watershed characterization, *Geophysics,* **73,** G7–G17.

Myer, D., Constable, S., Key, K., Glinsky, M.E. & Liu, G., 2012. Marine CSEM of the Scarborough gas field, Part 1: Experimental design and data uncertainty, *Geophysics,* **77,** E281–E299.

Nenna, V., Pidlisecky, A. & Knight, R., 2011. Informed experimental design for electrical resistivity imaging, *Near Surf. Geophys.,* **9,** 469–482.

Ogilvy, R.D. *et al.*, 2009. Automated monitoring of coastal aquifers with electrical resistivity tomography, *Near Surf. Geophys.,* **7,** 367–375.

Pollock, D. & Cirpka, O.A., 2010. Fully coupled hydrogeophysical inversion of synthetic salt tracer experiments, *Water Resour. Res.,* **46,** W07501, doi:10.1029/2009WR008575.

Radke, R.J., 2005. Image change detection algorithms: a systematic survey, *IEEE Trans. Image Process.,* **14,** 294–307.

Roux, E. & Garcia, X., 2014. Optimizing an experimental design for a CSEM experiment: methodology and synthetic tests, *Geophys. J. Int.,* **197,** 135–148.

Rucker, D., 2014. Investigating motion blur and temporal aliasing from time-lapse electrical resistivity, *J. appl. Geophys.,* **111,** 1–13.

Shang, X. & Huang, L., 2012. Optimal designs of time-lapse seismic surveys for monitoring CO$_2$ leakage through fault zones, *International Journal of Greenhouse Gas Control,* **10,** 419–433.

Singha, K. & Gorelick, S.M., 2005. Saline tracer visualized with three-dimensional electrical resistivity tomography: field-scale spatial moment analysis, *Water Resour. Res.,* **41,** W05023, doi:10.1029/2004WR003460.

Singha, K., Pidlisecky, A., Day-Lewis, F.D. & Gooseff, M.N., 2008. Electrical characterization of non-Fickian transport in groundwater and hyporheic systems, *Water Resour. Res.,* **44,** W00D07, doi:10.1029/2008WR007048.

Sjödahl, P., Dahlin, T. & Johansson, S., 2009. Embankment dam seepage evaluation from resistivity monitoring data, *Near Surf. Geophys.,* **7,** 463–474.

Slater, L., Binley, A., Versteeg, R., Cassiani, G., Birken, R. & Sandberg, S., 2002. A 3D ERT study of solute transport in a large experimental tank, *J. appl. Geophys.,* **49,** 211–229.

Stummer, P., Maurer, H. & Green, A.G., 2004. Experimental design: electrical resistivity data sets that provide optimum subsurface information, *Geophysics,* **69,** 120–139.

Stummer, P., Maurer, H., Horstmeyer, H. & Green, A.G., 2002. Optimization of DC resistivity data acquisition: real-time experimental design and a new multielectrode system, *IEEE Trans. Geosci. Remote Sens.,* **40,** 2727–2735.

Supper, R. *et al.*, 2014. Geoelectrical monitoring: an innovative method to supplement landslide surveillance and early warning, *Near Surf. Geophys.,* **12,** 133–150.

Uciński, D. & Patan, M., 2010. Sensor network design for the estimation of spatially distributed processes, *International Journal of Applied Mathematics and Computer Science,* **20,** 459–481.

Ward, A.S., Gooseff, M.N. & Singha, K., 2010. Imaging hyporheic zone solute transport using electrical resistivity, *Hydrol. Process.,* **24,** 948–953.

Wilkinson, P.B., Meldrum, P.I., Chambers, J.E., Kuras, O. & Ogilvy, R.D., 2006. Improved strategies for the automatic selection of optimized sets of electrical resistivity tomography measurement conffigurations, *Geophys. J. Int.,* **167,** 1119–1126.

Wilkinson, P.B., Chambers, J.E., Meldrum, P.I., Gunn, D.A., Ogilvy, R.D. & Kuras, O., 2010a. Predicting the movements of permanently installed electrodes on an active landslide using time-lapse geoelectrical resistivity data only, *Geophys. J. Int.,* **183,** 543–556.

Wilkinson, P.B., Meldrum, P.I., Kuras, O., Chambers, J.E., Holyoake, S.J. & Ogilvy, R.D., 2010b. High-resolution Electrical Resistivity Tomography monitoring of a tracer in a confined aquifer, *J. appl. Geophys.,* **70,** 268–276.

Wilkinson, P.B., Loke, M.H., Meldrum, P.I., Chambers, J.E., Kuras, O., Gunn, D.A. & Ogilvy, R.D., 2012a. Practical aspects of applied optimized survey design for electrical resistivity tomography, *Geophys. J. Int.,* **189,** 428–440.

Wilkinson, P.B., Chambers, J.E., Meldrum, P.I., Kuras, O. & Munro, C.J., 2012b. The robustness and general applicability of optimal resistivity surveys designed by maximising model resolution, in *Proceedings 18th European Meeting of Environmental and Engineering Geophysics,* Paris, France.

Xie, J., Clare, S., Gallichan, D., Gunn, R.N. & Jezzard, P., 2010. Real-time adaptive sequential design for optimal acquisition of arterial spin labeling MRI data, *Magn. Reson. Med.,* **64,** 203–210.

Zamuner, S., Di Iorio, V.L., Nyberg, J., Gunn, R.N., Cunningham, V.J., Gomeni, R. & Hooker, A.C., 2010. Adaptive-optimal design in PET occupancy studies, *Clinical Pharmacology & Therapeutics,* **87,** 563–571.